Zeolites

DOI: 10.1002/ange.201200317

Mesoporosity of Zeolite Y: Quantitative Three-Dimensional Study by Image Analysis of Electron Tomograms**

*Jovana Zečević, Cedric J. Gommes, Heiner Friedrich, Petra E. de Jongh, and Krijn P. de Jong**

Zeolites are crystalline microporous materials used, for example, as molecular sieves in separation and as solid catalysts in a multitude of industrial processes.[1–3] The micropores provide beneficial activity and shape selectivity, but can also set severe limitations on the diffusion of reactants and products.[4] Thus, different strategies have been developed in order to facilitate molecular transport to and from the active (micropore) sites. Essentially, most of the methods are based on reducing the size of the microporous regions by either the direct synthesis of smaller zeolite crystals (nanocrystals)[5,6] or by introducing mesopores (2–50 nm) throughout the zeolite crystal, dividing it into smaller microporous domains.[7–9] This reduces the diffusion path length and facilitates the mass transfer of molecules through the entire zeolite crystal. Assessing the parameters of the microporous domains and of the mesopore network is imperative for understanding the reaction kinetics coupled to molecular diffusion.[10–14]

For many years, zeolite Y has been a leading catalyst in industrial processes for oil refining and in petrochemistry, for example for fluid catalytic cracking, hydrocracking, and alkylation.[15] Zeolite Y owes this eminent role to its acidic nature, its crystalline structure composed of micropores (with so-called super cages 1.2 nm in diameter), and its pronounced stability under harsh reaction conditions. However, in the case of oil cracking, the retention of product molecules within the zeolite crystals caused by slow mass transfer through micropores can lead to secondary cracking and thereby formation of undesirable coke and gas products. Therefore, it is common practice to introduce mesopores in zeolite Y, mainly by steaming and acid leaching,[16–18] and more recently, by additional base leaching.[19,20] Mesoporosity is most frequently characterized using N_2 physisorption, which provides micropore and mesopore volumes and pore size distributions, while information on the shape of the mesopores, for example, cavity-like, ink-bottle-like, or channel-like, can sometimes be inferred from the shape of the physisorption isotherms.[21] However, the exact architecture of the mesopore network (shape, connectivity, and three-dimensional (3D) distribution of the mesopores) within a single crystal remains unknown, especially when complex mesopore networks, consisting of different types of pores, are present. Transmission electron microscopy (TEM) visualizes mesoporosity within a single crystal, but since the three-dimensional pore morphology is overlapping in a two-dimensional TEM micrograph, the obtained information is often insufficient and perhaps misleading. The pioneering work of A. H. Janssen et al.[17] in the field of electron tomography (ET also referred to as 3D-TEM) in heterogeneous catalysis provided a solution to this problem. They were able to visualize the interior of the USY (UltraStable Y) zeolite crystal and qualitatively described the shape and connectivity of the mesopores in three dimensions. Following this study, U. Ziesse et al.[22] employed image processing to extract quantitative information on the mesopore size distribution within this reconstructed zeolite crystal. Other electron tomography studies used image processing to also characterize the metal particles in heterogeneous catalysts.[23–27]

Here we combine the power of electron tomography (ET) with advanced image analysis operations to derive quantitative detailed information on the mesopore network of an industrially relevant mesoporous zeolite Y material. This approach enables us to distinguish and quantify structural characteristics of zeolite Y and its complex mesopore network. Some of this information is not accessible by techniques other than ET, such as the size distribution of the intact microporous domains, which plays an important role in the analysis of catalysis results.

For our study we used a commercially available steamed and acid-leached zeolite Y (CBV760, Zeolyst), which was in H-form and had a Si/Al ratio of 30, and is hence referred to as HY30. Firstly, the porosity of the bulk HY30 sample was examined using N_2 physisorption. The hysteresis loop in the adsorption–desorption isotherms (Figure 1, inset) is ascribed to capillary condensation effects and reveals the presence of mesopores. At higher relative pressures ($P/P_o > 0.8$) the adsorption and desorption branches of the isotherm are nearly parallel, suggesting that the mesopores are mainly open and channel-like. However, the sudden closure of the

[*] J. Zečević, Dr. P. E. de Jongh, Prof. Dr. K. P. de Jong
Inorganic Chemistry and Catalysis, Department of Chemistry
Utrecht University
Universiteitweg 99, 3584 CG Utrecht (The Netherlands)
E-mail: k.p.dejong@uu.nl
Dr. C. J. Gommes
Department of Chemical Engineering, Université de Liège B6A (Belgium)
Dr. H. Friedrich
Laboratory of Materials and Interface Chemistry, Department of Chemical Engineering and Chemistry, Eindhoven University of Technology (The Netherlands)

[**] J.Z., H.F., and K.P.de J. acknowledge support from the Dutch National Research School Combination Catalysis (NRSCC) and from NWO-CW. C.J.G. was supported by the Fonds de la Recherche Scientifique (F.R.S.-FNRS, Belgium). The Electron Tomography studies were carried out in the 3D Electron Microscopy group of Utrecht University headed by Dr. Willie Geerts and Dr. Jan Andries Post, with help from Hans Meeldijk. Dr. Gonzalo Prieto and Ad Mens were involved in physisorption.

Supporting information for this article is available on the WWW under http://dx.doi.org/10.1002/anie.201200317.

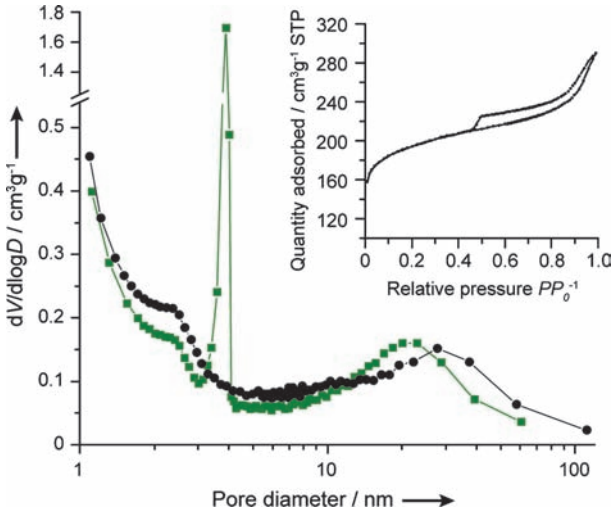

Figure 1. N_2 physisorption analysis of the HY30 sample. The inset shows adsorption and desorption isotherms with a hysteresis loop which is indicative of the presence of mesopores, while the sudden closure at about 0.45 relative pressure implies that some of the mesopores are blocked ("closed" and/or constricted). The Barrett–Joyner–Halenda pore size distribution (PSD) derived from the desorption branch data (green) depicts a sharp peak at 4 nm, assigned to blocked mesopores. Both desorption (green) and adsorption (black) branches show a broad mesopore size distribution with a mean value of roughly 20–30 nm.

hysteresis loop at $P/P_o = 0.45$ points to cavitation resulting from the presence of blocked mesopores that can only be accessed either through micropores ("closed" mesopores) or through openings with a diameter of less than 4 nm (constricted mesopores). Consequently, the pore size distribution curve (PSD) derived from the desorption branch using the Barrett–Joyner–Halenda (BJH) model exhibits a sharp peak at about 4 nm, while this peak is absent in the PSD curve derived from the adsorption branch (Figure 1). As there is no evidence for mesopores 4 nm in diameter, this sharp peak is ascribed instead to blocked mesopores and is used to calculate their volume. The type of the blockage ("closed" or constricted) and the size of those mesopores cannot, however, be identified using the available models.[21,28]

Furthermore, the adsorption branch shows a relatively broad PSD, with a mean pore size of about 30 nm in diameter. Another peak rising just above 2 nm in both the adsorption and desorption PSD curves suggests the existence of very small mesopores; however, determining their volume would be unreliable because of the limitations of the BJH model. Clearly, in the case of more complex pore networks such as this one, N_2 physisorption fails to reveal important features of the mesopore network, including the type and size of the blocked mesopores, the shape of the channel-like mesopores (straight or curved), and their interconnectivity and orientation within the zeolite crystal. Therefore, we have carried out an electron tomography study which has met with great success in visualizing mesopore networks in solid catalysts.[17,18]

Electron tomography (ET)[29,30] is based on acquiring multiple TEM images of an object from different directions, and using the information from all the TEM images to calculate (by back-projection) a reconstruction of the object (a 3D intensity map). The clear advantage of ET over conventional TEM imaging is evident in Figure 2. The TEM image of the zeolite crystal (Figure 2a) displays the mesopores as brighter features pervading the crystal, yet without a clear indication of their shapes, sizes, and connectivity, since

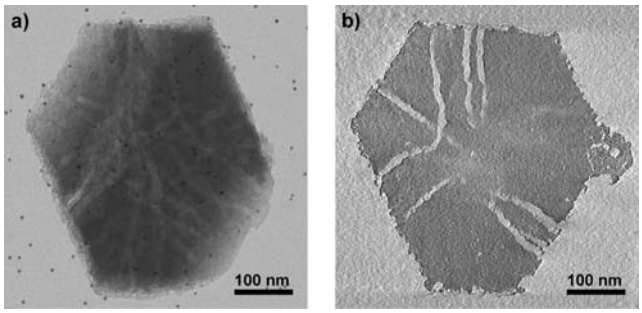

Figure 2. Electron microscopy and electron tomography study of the HY30 sample. a) TEM micrograph at a tilt angle of 31°, indicating the presence of a complex mesopore network. b) A virtual slice from the middle of the reconstructed volume obtained by electron tomography clearly depicts the presence of channel-like mesopores distributed throughout the crystal.

their 3D morphology is overlapping in the 2D image. A slice taken from the middle of the 3D reconstruction of the same particle (Figure 2b) clearly distinguishes channel-like mesopores (light gray) that are spread throughout the zeolite crystal (dark gray) connecting inner microporous parts to the outer surface. Detailed observation of the whole reconstructed volume (Movie 1 in the Supporting Information) reveals that most of the mesopore channels are interconnected, with a few "closed" spherical mesopores also present. Moreover, electron tomography exposes additional features, such as an apparent preferential growth direction of the mesopores within the crystal, as well as very small pores (ca. 2 nm, also implied from N_2 physisorption). These findings are unambiguously valuable for understanding the architecture of the mesopore network; however, detailed quantification of the visualized network is required. Manual segmentation and quantification of features of interest is labor intensive and susceptible to errors and bias; hence automated image processing is preferred when large data files such as 3D reconstructions need to be processed.

The first step of image processing involved segmenting the elements of interest from the 3D reconstructed volume, that is, determining for each voxel whether it belongs to the mesopore and background or to the microporous solid. This was done by morphological filtering followed by thresholding, which results in a binarized reconstruction from which the mesopore networks were successfully isolated. The segmentation algorithm was designed so as to preserve any feature of the reconstruction with a size larger than 2 nm (see the Supporting Information). An example of such a sequence of operations followed by volume and isosurface rendering, which enhance the features of interest and facilitate visualization of the internal morphology, is shown in Movie 2 in the

Supporting Information. The movies, as well as the presented figures, depict one of the two HY30 crystals that were imaged and analyzed, while the quantification results comprise data from both crystals. More detailed information on the image processing and a comparative study of two imaged crystals can be found in the Supporting Information.

Based on the segmented reconstruction, we were able to define and quantify the important properties of the mesopore network with regard to its accessibility. Mesopores that are accessible from the outer surface of the crystal through the mesopore network (open mesopores) were distinguished from the "closed" ones that can be reached only through micropores. Figure 3a,b depict segmented mesopores of one of two analyzed crystals, where, as can be visually inferred, open porosity (green) dominates over "closed" porosity (red). Moreover, the irregular shape of the mesopores, and hence

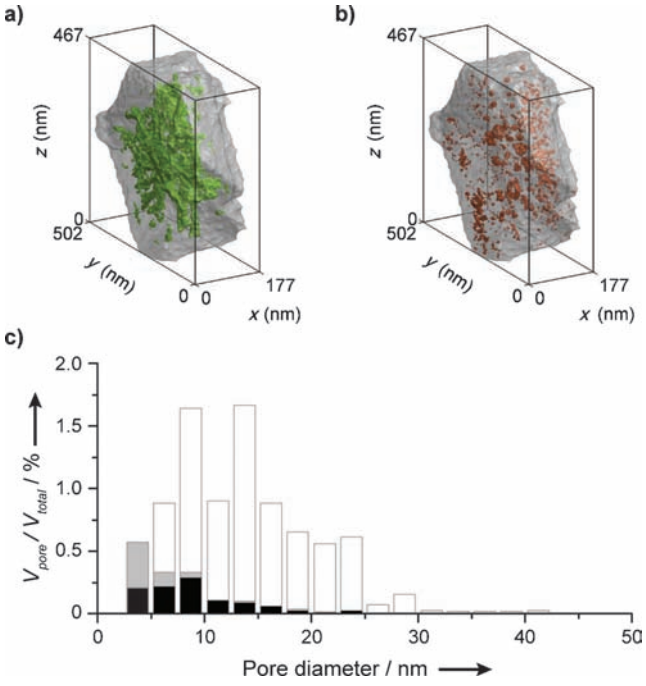

Figure 3. Accessibility of the mesopores described and quantified using image processing. Volume-rendered 3D representations of the open mesopores in green (a) and the "closed" mesopores in red (b) visually suggest that an open type of porosity prevails. c) Pore size distribution of open mesopores (white), constricted mesopores (gray), and "closed" mesopores (black) defined as V_{pore}/V_{total}, where V_{pore} corresponds to the volume of considered types of mesopores and V_{total} to the total volume of the zeolite crystal.

the varying diameter, implies that some of the mesopores can be reached from the outer surface only through narrower openings, the width of which is referred to as the breakthrough diameter (Figure S1 in the Supporting Information). The latter notion enabled us to consider a second type of blocked mesopores: we define a constricted pore as a mesopore having a breakthrough diameter less than 4 nm. In other words, image processing enabled us to discern and measure two types of blocked mesopores ("closed" and constricted), which are indistinguishable and whose size cannot be resolved by the N_2 physisorption analysis. After the volumes and diameters of above-defined mesopores (Figure 3c) were determined, a direct comparison with N_2 physisorption results becomes possible (Table 1).

Considering the fact that N_2 physisorption measures porosity of a bulk sample (approximately 10^{12} crystals) while image analysis was performed on only two crystals,

Table 1: Comparison of the mesoporosity derived from image analysis and that from N_2 physisorption.

	V_{meso}[a] [%]	V_{constr}[b] [%]	V_{closed}[c] [%]	$V_{blocked}$[d] [%]
Image analysis	9	6	12	18
N_2 physisorption	15	–	–	22

[a] Percentage of total mesoporosity (V_{meso}) within zeolite crystals defined as V_{meso}/V_{total}, where V_{total} represents the total volume of the zeolite crystal. [b] Percentage of constricted type of mesopores defined as V_{constr}/V_{meso}. [c] Percentage of "closed" mesopores defined as V_{closed}/V_{meso}. [d] Percentage of blocked mesopores defined as $V_{blocked}/V_{meso}$, where $V_{blocked} = V_{constr} + V_{closed}$.

the obtained volume percentages were surprisingly similar, which suggests homogeneity of the sample. The same holds for the pore size distribution (Figure 3c), from which it is apparent that the imaged crystals have somewhat smaller mesopore diameters compared to the bulk sample (Figure 1). Interparticle porosity in the measured zeolite powder cannot be excluded which would shift the PSD to larger diameters and increase the pore volume.

The mass transfer efficiency of the mesopore network greatly depends on how curved, that is, how tortuous the mesopore channels are.[31] The tortuosity can be quantified by comparing the following two distances defined for any given point in the pore space (Figure 4). The first is the straight-line or Euclidean distance L_E to the surface of the crystal; the second is the length of the shortest path *within the mesopore space* that connects the point to the surface. The latter length is referred to as the geodesic distance L_G. Figure 4c compares systematically L_G to L_E for all mesopore voxels of the two reconstructions. The slope of this line represents the tortuosity of the mesopore space, which is 1.3 for HY30 zeolite. This tortuosity can be visually perceived from Figure 2b and from Movies 1 and 2 in the Supporting Information.

Finally, as indicated before, mesopores are primarily introduced in order to "break" the crystal into smaller microporous domains, which shortens diffusion path length and, hence, reduces the residence time of molecules within micropores. Knowing the size of the microporous domains would be beneficial for understanding the molecular diffusion and subsequent reactions, and also for judging the effectiveness of the introduced mesopore networks. A first estimate of the size of microporous domains is derived from the ratio of their volume to the external surface area (V/S). In our case, the volume was defined as the reciprocal of the zeolite density ($\rho = 0.958\ g\,cm^{-3}$), and the external surface area was calculated using a t-plot from physisorption ($S = 213\ m^2\,g^{-1}$). This leads to an equivalent sphere radius ($r_s = 3\,V/S$) of 15 nm. The equivalent radius calculated from image analysis is 36 nm.

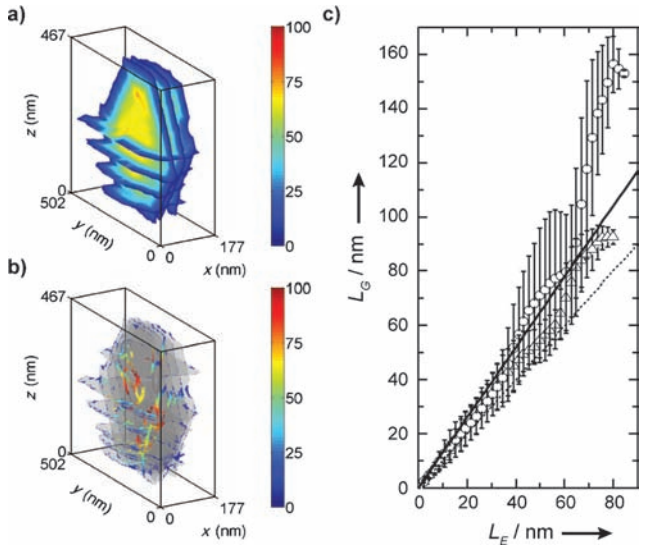

Figure 4. Tortuosity of the mesopore network derived from image analysis. a) Color map of the shortest distances from any point of the crystal to the surface of the crystal (Euclidean distances L_E). b) Color map of the actual distances from any point within mesopores to the surface of the crystal (geodesic distances L_G). c) Plotted Euclidean (L_E) and geodesic distances (L_G) for all voxels of the two reconstructions (distinguishable by circle and triangle symbols); the error bars are the standard deviation of L_G for all voxels having a given L_E. The slope of the fitted straight line (full) deviates from the value of 1 (dotted), indicating a slightly tortuous mesopore network. Color bars refer to distances in nm.

The difference between the two values points to a significant mesopore surface roughness, which leads to an overestimation of the external geometrical surface area of the microporous domains. This observation further stresses the need for image analysis. Equally important for hydrocracking reactions is the width of the size distribution, which determines the selectivity of the catalyst. This information can be obtained through image analysis by measuring the distance between any point in the micropore region and the closest mesopore surface (Figure 5). The distance distribution shows that 90% of the points of the microporous crystallite are within 15 nm from a mesopore. However, when these distances are reduced to even less than 15 nm a remarkable improvement of hydrocracking selectivity takes place. This was achieved by base leaching of HY30, which induced a whole new network of small mesopores, and hence, successfully divided the crystal into smaller microporous domains.[19] It would be very difficult to measure the characteristics of microporous domains by any other means than image analysis.

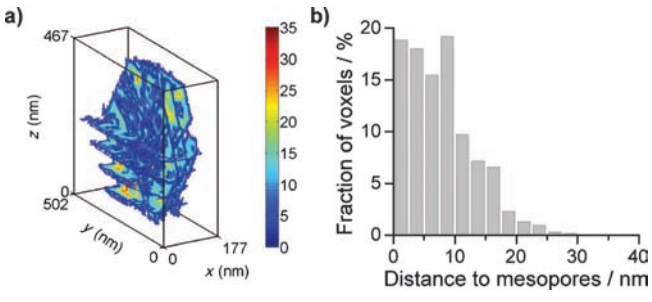

Figure 5. Size distribution of microporous domains created upon introduction of mesopores. a) Color map of the shortest distances from any point of a micropore region to the nearest mesopore surface. b) Size distribution of the microporous domains defined as a fraction of the voxels of microporous region with a corresponding shortest distance to the mesopore surface. Color bar refers to distances in nm.

We derived 3D reconstructed volumes of zeolite Y and its mesopore network with nanometer resolution, which enabled image analysis to isolate and measure two types of blocked mesopores ("closed" and constricted mesopores), the tortuosity of the mesopores, and the size distribution of unaffected microporous domains. The results from combining electron tomography with image analysis provide quantitative data on the morphology of mesoporous zeolites which cannot be obtained by any other technique. This approach establishes a new basis for the quantitative interpretation of the impact of mesoporosity and molecular diffusion on catalyst activity, selectivity, and stability.

Experimental Section

Commercially available mesoporous zeolite Y, previously steamed and acid leached, was purchased from Zeolyst under the sample code CBV760. N_2 physisorption measurements were carried out on Micrometrics Tristar 3000 at liquid-nitrogen temperature. Prior to measurement, samples were degassed under nitrogen flow at 300 °C for 14 h. Electron tomography of selected zeolite particles was performed on a Tecnai 20 (FEI) instrument in a bright-field imaging mode at 200 kV. A series of tilt images were acquired at nominal magnification of 29000 times over an angular range of about ± 75° at increments of 1 or 2°. Alignment of the acquired tilt series and subsequent reconstructions were performed using IMOD software package.[32] Image analysis was performed with Matlab using the SDC mathematical morphology toolbox.

Received: January 12, 2012
Published online: March 15, 2012

Keywords: electron tomography · image processing · mesoporous materials · microporous materials · zeolites

[1] A. Corma, *Chem. Rev.* **1997**, *97*, 2373 – 2419.
[2] C. R. Marcilly, *Top. Catal.* **2000**, *13*, 357 – 366.
[3] J. Weitkamp, *Solid State Ionics* **2000**, *131*, 175 – 188.
[4] D. M. Ruthven, M. F. M. Post, *Stud. Surf. Sci. Catal.* **2001**, *137*, 525 – 577.
[5] M. Choi, K. Na, J. Kim, Y. Sakamoto, O. Terasaki, R. Ryoo, *Nature* **2009**, *461*, 246 – 249.
[6] L. Tosheva, V. P. Valtchev, *Chem. Mater.* **2005**, *17*, 2494 – 2513.
[7] J. Pérez-Ramírez, C. H. Christensen, K. Egeblad, C. H. Christensen, J. C. Groen, *Chem. Soc. Rev.* **2008**, *37*, 2530 – 2542.
[8] K. Egeblad, C. H. Christensen, M. Kustova, C. H. Christensen, *Chem. Mater.* **2008**, *20*, 946 – 960.
[9] M. Choi, H. S. Cho, R. Srivastava, C. Venkatesan, D.-H. Choi, R. Ryoo, *Nat. Mater.* **2006**, *5*, 718 – 723.
[10] J. Kärger et al., *Chem. Eng. Technol.* **2009**, *32*, 1494 – 1511.
[11] R. Valiullin, S. Naumov, P. Galvosas, J. Kärger, H.-J. Woo, F. Porcheron, P. A. Monson, *Nature* **2006**, *443*, 965 – 968.
[12] G. Wang, E. Johannessen, C. R. Kleijn, S. W. de Leeuw, M.-O. Coppens, *Chem. Eng. Sci.* **2007**, *62*, 5110 – 5116.

[13] D. Tzoulaki, L. Heinke, W. Schmidt, U. Wilczok, J. Kärger, *Angew. Chem.* **2008**, *120*, 4018 – 4021; *Angew. Chem. Int. Ed.* **2008**, *47*, 3954 – 3957.
[14] P. Kortunov et al., *J. Am. Chem. Soc.* **2005**, *127*, 13055 – 13059.
[15] W. Vermeiren, J.-P. Gilson, *Top. Catal.* **2009**, *52*, 1131 – 1161.
[16] R. A. Beyerlein, C. Choi-Feng, J. B. Hall, B. J. Huggins, G. J. Ray, *Top. Catal.* **1997**, *4*, 27 – 42.
[17] A. H. Janssen, A. J. Koster, K. P. de Jong, *Angew. Chem.* **2001**, *113*, 1136 – 1138; *Angew. Chem. Int. Ed.* **2001**, *40*, 1102 – 1104.
[18] A. H. Janssen, A. J. Koster, K. P. de Jong, *J. Phys. Chem. B* **2002**, *106*, 11905 – 11909.
[19] K. P. de Jong, J. Zečević, H. Friedrich, P. E. de Jongh, M. Bulut, S. van Donk, R. Kenmogne, A. Finiels, V. Hulea, F. Fajula, *Angew. Chem.* **2010**, *122*, 10272 – 10276; *Angew. Chem. Int. Ed.* **2010**, *49*, 10074 – 10078.
[20] D. Verboekend, G. Vilé, J. Pérez-Ramírez, *Adv. Funct. Mater.* **2012**, DOI: 10.1002/adfm.201102411.
[21] J. C. Groen, L. A. A. Peffer, J. Pérez-Ramírez, *Microporous Mesoporous Mater.* **2003**, *60*, 1 – 17.
[22] U. Ziese, C. J. Gommes, S. Blacher, A. H. Janssen, A. J. Koster, K. P. de Jong, *Stud. Surf. Sci. Catal.* **2005**, *158*, 633 – 638.
[23] C. J. Gommes, K. de Jong, J.-P. Pirard, S. Blacher, *Langmuir* **2005**, *21*, 12378 – 12385.
[24] O. Ersen, J. Werckmann, M. Houllé, M.-J. Ledoux, C. Pham-Huu, *Nano Lett.* **2007**, *7*, 1898 – 1907.
[25] H. Friedrich, J. R. A. Sietsma, P. E. de Jongh, A. J. Verkleij, K. P. de Jong, *J. Am. Chem. Soc.* **2007**, *129*, 10249 – 10254.
[26] J. C. González, J. C. Hernández, M. López-Haro, E. del Río, J. J. Delgado, A. B. Hungría, S. Trasobares, S. Bernal, P. A. Midgley, J. J. Calvino, *Angew. Chem.* **2009**, *121*, 5417 – 5419; *Angew. Chem. Int. Ed.* **2009**, *48*, 5313 – 5315.
[27] R. Grothausmann et al., *J. Am. Chem. Soc.* **2011**, *133*, 18161 – 18171.
[28] J. C. Groen, J. Pérez-Ramírez, *Appl. Catal. A* **2004**, *268*, 121 – 125.
[29] P. A. Midgley, E. P. W. Ward, A. B. Hungría, J. M. Thomas, *Chem. Soc. Rev.* **2007**, *36*, 1477 – 1494.
[30] H. Friedrich, P. E. de Jongh, A. J. Verkleij, K. P. de Jong, *Chem. Rev.* **2009**, *109*, 1613 – 1629.
[31] C. J. Gommes, A.-J. Bons, S. Blacher, J. H. Dunsmuir, A. H. Tsou, *AIChE J.* **2009**, *55*, 2000 – 2012.
[32] J. R. Kremer, D. N. Mastronarde, J. R. McIntosh, *J. Struct. Biol.* **1996**, *116*, 71 – 76.

